Table 1, c_0 the characteristic speed is $c_0 = \dfrac{k_0}{\mu_f \phi_0}\Delta\rho g$, the error is not propagated in the text.

Eq 10 should read $\dfrac{\partial\phi}{\partial t} = -\left(1-\phi\right)\dfrac{p_e}{\zeta} - v_s\nabla\phi$, the error is not propagated in the text.

Paragraph 25: Second sentence: "and inference" should read "an inference". Last sentence should read: In such settings, the probable effect of far-field stresses would be to flatten the channels into …

Paragraph 37: The time-averaged excess flux, i.e., the fluid flux in excess of the background flux ($c_0\phi_0$), associated with the passage of a 1-dimensional wave is $\omega/\lambda\cdot(F-1)$ and not $\omega\cdot(F-1)$ as stated in the text. This error is propagated in Equations 41 and 42, which should be corrected accordingly.

Paragraph 44: the relation $t^*(y) \sim 6\sqrt{\mu}\big/\phi_0$ is for fluid viscosity μ in Pa-s.

Decompaction weakening and channeling instability in ductile porous media: Implications for asthenospheric melt segregation

J. A. D. Connolly[1] and Y. Y. Podladchikov[2]

[1]   We propose that a mechanical flow channeling instability, which arises because of rock weakening at high fluid pressure, facilitates segregation and transport of asthenospheric melts. To characterize the weakening effect, the ratio of the matrix viscosity during decompaction to that for compaction is treated as a free parameter R in the range 1 to 10^{-6}. Two-dimensional numerical simulations with this rheology reveal that solitary, vertically elongated, porosity waves with spacing on the compaction length scale δ initiate from miniscule porosity perturbations. By analogy with viscous compaction models we infer that in the absence of far-field stress, the three-dimensional expression of the waves is as pipe-like structures of radius $\delta\sqrt{R}$, a geometry that increases fluid fluxes by a factor of $\sim 1/R$. The waves grow by draining fluid from the background porosity but leave a wake of elevated porosity that localizes subsequent flow. Wave amplitudes grow linearly with time, increasing by a factor of $R^{-3/8}$ in the time required to drain the porosity a distance of $\sim\delta$. Dissipation of gravitational potential energy by the waves has the capacity to enhance growth rates through melting. Maximum wave speeds are ~ 40 times the speed of fluid flow through the unperturbed matrix. Such waves may provoke the elastic response necessary to nucleate, and localize the melt necessary to sustain, more effective transport mechanisms. The formulation introduces no melting effects and is applicable to fluid flow and localization problems in ductile porous media in general.

1.   Introduction

[2]   No satisfactory explanation has been offered for the transition from pervasive to segregated melt transport in ductile rocks. In the simplistic extreme, pervasive processes exploit existing porosity, whereas segregated transport is a mechanism in which the melt moves through a void space that propagates or grows dynamically. Although the latter mechanism may be realized as self-propagating melt-filled cracks, the critical crack length is too long to permit the cracks to initiate spontaneously from a matrix in which melt is pervasively distributed [*Rubin*, 1998]. Thus an intermediate mechanism capable of bridging the extremes between pervasive and segregated transport is required, at least, to explain the initial stages of melt segregation. Porosity waves are such a mechanism [*Scott and Stevenson*, 1984; *Richter and McKenzie*, 1984], but the popularity of the porosity wave model has declined because of the perception that pervasive fluid transport is too inefficient to be significant on the time and spatial scales relevant for melt segregation

and transport [*Slater et al.*, 2001; *McKenzie*, 2000]. This failing may in part be attributed to the rheological model used to evaluate the relevance of the porosity wave mechanism. In previous work [*Connolly and Podladchikov*, 1998] we have shown that rheological asymmetry leads to a mechanical flow channeling instability. Here we present a numerical study undertaken to characterize the instability. The results demonstrate that the instability can nucleate from miniscule perturbations to an initially uniform porosity and that it grows by drawing fluid from the surrounding matrix. The instability offers a mechanism both for collecting small amounts of melt and for disaggregation of the matrix to form a magmatic suspension.

[3]   In the present context, disaggregation is taken to represent the transition from fluid flow through a coherent matrix to one in which the matrix is fluidized so that it is no longer possible to distinguish separate solid and fluid pressure fields. In detail this transition is likely to be complex and material-dependent, but theoretical and experimental considerations suggest the transition occurs at porosities of $\phi \sim 20\%$ [*Arzi*, 1978; *Ashby*, 1988; *Auer et al.*, 1981]. Our concern is the mechanism by which the melt fractions necessary to provoke this transition are achieved, rather than the transition itself. To this end, we adopt a small porosity formulation $(1 - \phi \to 1)$ that allows us to study the hydraulic character of flow instabilities without considering the details of the matrix deformation. *Scott* [1988], and *Scott*

―――――――
[1]Earth Sciences Department, ETH Zurich, Zurich, Switzerland.
[2]Physics of Geological Processes, University of Oslo, Blindern, Oslo, Norway.
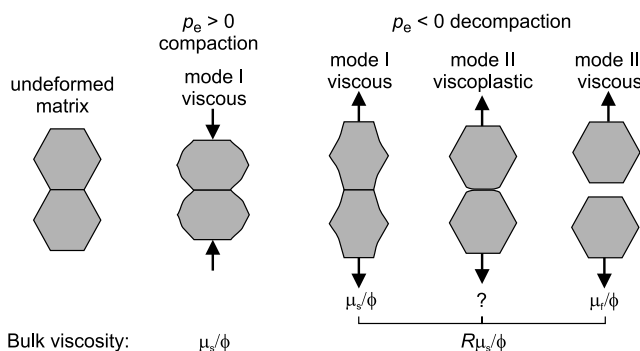
Figure 1. Schematic rheology with three modes of microscopic deformation: mode I, viscous deformation of solid grains; mode II, viscoplastic failure of coherent grain boundaries; mode III, and opening of noncohesive grain boundaries. We assume that modes II and III are less likely to occur during compaction ($p_e > 0$) and therefore that the fluid-matrix aggregate is weaker in decompaction ($p_e < 0$). The simplest model for pure mode I deformation that satisfies the physical requirement that the viscosity must be infinite in the limit $\phi \to 0$ is $\zeta \sim \mu_s/\phi$, where η_s is the solid shear viscosity [*Nye*, 1953; *Sumita et al.*, 1996]. In contrast, mode III decompaction is limited by the rate at which fluid is able to fill newly created porosity (i.e., viscous). At small porosities the drag force resisting this flow will be proportional to fluid shear viscosity (μ_f) and inversely proportional to porosity; thus it is reasonable to expect that for mode III, $\zeta \sim \mu_f/\phi$. Considering only these two modes gives an admissible variation in effective bulk viscosity as large as the difference between the fluid and matrix shear viscosities. Mode II will be operative at effective stresses comparable to cohesion and is likely to involve complex viscoplastic interactions. To account for the combined effects of all three modes, we parameterize the effective viscosity for decompaction as $\zeta = R\mu_s/\phi$, where $R < 1$.

and Stevenson [1986], also *Schmeling* [2000] isolated the effect of matrix deformation and showed that it enhances the growth rate and speed of porosity waves, but that it does not fundamentally change the scales governing wave propagation and stability for parameter ranges relevant to the asthenosphere. More complex formulations that extend to large porosity [*Bercovici et al.*, 2001; *Rabinowicz et al.*, 2001] are capable of describing disaggregation, but contain no features that would hinder the formation of waves with porosities comparable to that at which disaggregation is thought to occur. The formulation of *Bercovici et al.* [2001] reduces to the formulation used here in the small porosity limit provided surface tension is negligible. Although surface tension is poorly quantified, it will be most significant at small porosity and is therefore a potentially important term that is neglected here.

[4] Reactive infiltration instability [*Daines and Kohlstedt*, 1994; *Aharonov et al.*, 1995] and shear-enhanced melt segregation [*Holtzman et al.*, 2003] are mechanisms for melt segregation that have recently received attention in the context of melt flow beneath mid-ocean ridges. Although quantitative modeling suggests that the reactive infiltration instability leads to relatively weak amplification of back-ground melt fluxes, and is therefore unlikely to cause complete segregation, it provides a largely consistent model for mid-ocean ridge melt chemistry [*Spiegelman et al.*, 2001]. The relevance of the reactive infiltration instability to other geodynamic settings is less clear because it requires that the stability of the melt increases in the transport direction. Thus it is unlikely to operate in the vicinity of the lithospheric transition and in the lower asthenosphere where melting may be controlled by chemical heterogeneity [*Plank and Langmuir*, 1992; *Hirth and Kohlstedt*, 1996; *Phipps Morgan and Morgan*, 1999]. Shear-enhanced segregation is not yet well understood on a theoretical basis, but experimental and mathematical models suggest that large strains may be required to achieve moderate amplifications [*Holtzman et al.*, 2003; *Spiegelman*, 2003; *Rabinowicz and Vigneresse*, 2004; *Phipps Morgan and Holtzman*, 2005; *Petford et al.*, 2005]. Thus a case can be made for the necessity of a mechanism that is dependent only on the inherent mechanical instability of an interconnected fluid in a ductile matrix. Particularly in the lower asthenosphere, such instabilities must grow rapidly in order to compete with diffusive processes that reduce the stability of the melt [*Hofmann and Hart*, 1978; *Kogiso et al.*, 2004]; the mechanical instability proposed here grows linearly with time and therefore has the potential to meet this criterion. Porosity waves initiate in response to a flow obstruction, such that both the amplitude and speed of the waves are proportional to the magnitude of the obstruction [*Spiegelman*, 1993; *Connolly and Podladchikov*, 1998]. Since melt fractions produced by adiabatic upwelling of mantle material are expected to be relatively homogeneous [*McKenzie*, 1985; *Scott and Stevenson*, 1986], it can be argued that the obstructions necessary to nucleate porosity waves are small or entirely absent within the asthenosphere. Thus an important issue to be addressed in the present analysis is the magnitude of the heterogeneities necessary to trigger porosity waves.

[5] Objections premised on the inefficiency of porosity waves as a transport mechanism are based upon mechanical and analogue models in which compaction and decompaction are symmetrical processes. However, physical intuition suggests that this is unlikely to be true for granular materials such as porous rock [*Connolly and Podladchikov*, 1998; *Ricard and Bercovici*, 2003]. In rocks, decompaction is accomplished by viscous deformation of individual grains and by opening grain boundaries, whereas compaction occurs primarily by the former mechanism (Figure 1). The observation that rocks possess macroscopic cohesive strengths of $O(10)$ MPa [*Gueguen and Palciauskas*, 1994] suggests that individual grain boundaries must have finite strength and therefore that decompaction occurs by a mixture of plastic (i.e., rate-independent failure) and viscous deformation. Provided these modes operate in parallel the effective rheology is rate-dependent creep [*Sonder et al.*, 1986], but with an effective viscosity that is reduced compared to the viscosity that controls compaction. This model is designated hereafter as decompaction weakening. Assuming the existence of such a rheology, we begin by outlining a mathematical formulation of the problem and the numerical techniques used to resolve it. Numerical models are then used to develop an understanding of the instability and to establish the nature of its temporal and spatial

Table 1. Common Symbols and Characteristic Values Adopted for Purposes of Dimensional Argumentation[a]

Symbol	Meaning	Value
A	dimensionless amplitude (maximum porosity)	
C_p	isobaric heat capacity (pyrolite)	4×10^6 J K^{-1} m^{-3}
f	dimensionless porosity, ϕ/ϕ_0	
F	dimensionless excess fluid volume, equation (28)	
k	permeability, equation (14)	
k_0	background permeability	$10^{-7}\phi_0{}^n$ m^2
L	latent heat of melting	10^9 J m^{-3}
m	porosity exponent in bulk viscosity function, equation (12)	1
n	porosity exponent in permeability function, equation (14)	3
p	dimensionless fluid overpressure, $-p_e/(\delta\Delta\rho g)$	
p_e	effective pressure, $\bar{\sigma} - p_f$	
p_f	fluid pressure	
R	viscosity contrast	
t_c	dimensionless time, time/$t*$	
$t*$	compaction timescale, δ/c_0	10^3 years
V	dimensionless volume, volume/δ^3	
v_s	solid velocity	
v_f	fluid velocity	
c_0	magnitude of v_f at $p_e = 0$ and $\phi = \phi_0$, $k_0\Delta\rho g/\mu_f$	10^{-1}, 1 m yr^{-1}
z	upward directed vertical coordinate	
δ	compaction length scale, $\sqrt{k_0\mu_s/\phi_0^m/\mu_f}$	10^3 m
$\Delta\rho$	difference between solid and fluid density	500 kg m^{-3}
μ_s	solid shear viscosity	10^{18} Pa s
λ	dimensionless length scale for porosity	
ϕ	porosity	
ϕ_0	background porosity	10^{-3}, 10^{-2}
$\bar{\sigma}$	mean stress, equation (5)	
μ_f	fluid shear viscosity	10^{-1}, 10 Pa s
ω	dimensionless wave speed c/c_0	
ζ	aggregate bulk viscosity, equation (13)	

[a]Where two values are given, the first is the value adopted for the lower asthenosphere, where melting is presumed to be caused by water-rich heterogeneities that result in the formation of low-viscosity melts, the viscosities expected of such melts vary from $O(10^0)$ Pa s for basaltic melt to $O(10^{-1})$ Pa s for kimberlitic melt. The second value is for basaltic melts generated in the upper asthenosphere (<~60 km depth) beneath mid-ocean ridges. In the lower asthenosphere, background porosities of $O(10^{-3})$ are necessary to explain chemical fractionation patterns [McKenzie, 1985; Khazan and Fialko, 2005]. Beneath mid-ocean ridges, melt viscosities are of $O(10^1)$ Pa s and geophysical and geochemical [Forsyth et al., 1998; Spiegelman and Reynolds, 1999] evidence is consistent with background porosities of $O(10^{-2})$. The compaction scales have been rounded to the nearest order of magnitude to emphasize the approximate character of the scales.

scaling. We conclude with a discussion of its implications in the context of asthenospheric melting.

2. Mathematical Formulation

[6] In essence, we follow the formulation of Scott and Stevenson [1984, 1986] for Darcyian flow of an incompressible fluid through a viscous matrix composed of incompressible solid grains. Although the solid and fluid components are incompressible, the matrix is compressible because fluid may be expelled from the pore volume. Conservation of solid and fluid mass then requires

$$\frac{\partial(1-\phi)}{\partial t} + \nabla \cdot [(1-\phi)v_s] = 0 \qquad (1)$$

and

$$\frac{\partial\phi}{\partial t} + \nabla \cdot (\phi v_f) = 0 \qquad (2)$$

where ϕ is porosity, and subscripts f and s distinguish the velocities, v, of the fluid and matrix (see Table 1 for notation). Equation (1) expands as

$$\frac{\partial\phi}{\partial t} = (1-\phi)\nabla \cdot v_s - v_s\nabla\phi \qquad (3)$$

revealing that variation in porosity arises through both dilation and advection of the matrix, i.e., the first and second terms of equation (3). From Darcy's law, the force balance between the matrix and fluid is

$$\phi(v_f - v_s) = -\frac{k}{\mu_f}\nabla\bar{p} \qquad (4)$$

where k is the matrix permeability, which is assumed to be scalar function of porosity; μ is the fluid viscosity, a constant; $\bar{p}$ is the fluid overpressure defined relative to hydrostatic conditions such that $\bar{p} = p_f + \rho_f gz$ with upward increasing depth coordinate z; and ρ_f is the fluid density. Approximating the mean stress $\bar{\sigma}$ as the vertical load

$$\bar{\sigma} \approx \bar{\sigma}_0 - \int_0^z \left[(1-\phi)\rho_s + \phi\rho_f\right]gdz \qquad (5)$$

equation (4) is written in terms of the effective pressure ($p_e = \bar{\sigma} - p_f$)

$$\phi(v_f - v_s) = \frac{k}{\mu_f}\left[\nabla p_e + (1-\phi)\Delta\rho gu_z\right] \qquad (6)$$

where $\Delta\rho = \rho_s - \rho_f$ and u_z is an upward directed unit vector. The isostasy assumption implicit in equation (5) is equivalent to the assumption that the shear viscosity of the matrix is negligible in comparison to the bulk viscosity. *Scott* [1988] and *Scott and Stevenson* [1986] evaluated the effect of this assumption by both linear stability and numerical analysis and discovered that finite shear viscosities influence porosity wave properties, but do not effect the qualitative behavior and scaling predicted from the compaction equations.

[7] The divergence of the total volumetric flux of matter is the sum of equations (1) and (2):

$$\nabla \cdot \left[v_s + \phi\left(v_f - v_s\right)\right] = 0 \tag{7}$$

and substituting equation (6) into equation (7) gives

$$\nabla \cdot \left(v_s + \frac{k}{\mu_f}[\nabla p_e + (1 - \phi)\Delta\rho g u_z]\right) = 0 \tag{8}$$

[8] Rheology is introduced through Terzaghi's effective stress principle as

$$\nabla \cdot v_s = -\frac{p_e}{\zeta} \tag{9}$$

where ζ, a function of porosity and effective pressure, is the bulk viscosity of the system. Substitution of equation (9) into equations (3) and (8) yields two equations in three unknowns $\{\phi, p_e, v_s\}$:

$$\frac{\partial \phi}{\partial t} = (1 - \phi)\frac{p_e}{\zeta} - v_s\nabla\phi \tag{10}$$

$$\frac{p_e}{\zeta} = \frac{1}{\mu_f}\nabla \cdot \{k[\nabla p_e + (1 - \phi)\Delta\rho g u_z]\} \tag{11}$$

that are usually closed by the introducing the matrix force balance equation. However, we show next that for the small porosity conditions of interest, dimensional considerations indicate that the porosity advection term in equation (10) is negligible in which case equations (12) and (13) reduce to a closed system of equations in $\{\phi, p_e\}$.

2.1. Constitutive Relations and Nondimensionalization

[9] Bulk viscosity is commonly approximated as

$$\zeta_c \approx \mu_s/\phi^m \tag{12}$$

where m is an exponent between zero and one and μ_s is the shear viscosity of the solid grains [*Scott and Stevenson*, 1984]. In contrast to most earlier studies that neglected the porosity dependence of the bulk viscosity, i.e., by explicitly or implicitly taking $m = 0$ in equation (12), we consider the case $m = 1$. This choice is theoretically justified in the small porosity limit [*Nye*, 1953; *Sumita et al.*, 1996], is consistent with both experimental [*Ashby*, 1988; *Renner et al.*, 2003] and natural [*Connolly and Podladchikov*, 2000] compaction profiles, and precludes unrealistic behavior such as negative porosity [*Connolly and Podladchikov*, 1998, 2000].

[10] To simulate the compaction-decompaction asymmetry, we express effective bulk viscosity (Figure 1) as a step function of effective pressure

$$\zeta = \zeta_c[R - H(p_e)(R - 1)] \tag{13}$$

where R is the ratio of bulk viscosity in decompaction ($R\zeta_c$) to that in compaction (ζ_c, equation (12)) and $H(p_e)$ is the Heaviside function. Permeability is expressed as

$$k = k_0\left(\frac{\phi}{\phi_0}\right)^n \tag{14}$$

where k_0 and ϕ_0 are the background values of the permeability and porosity, respectively, and the exponent n is taken to be a constant. Although $n = 3$ is assumed throughout this work, we retain the algebraic notation for generality.

[11] Appropriate scales for nondimensionalization are the background porosity, ϕ_0, the viscous compaction length

$$\delta \approx \sqrt{k_0\mu_s/\phi_0^m/\mu_f} \tag{15}$$

the characteristic compaction pressure

$$p^* = \delta\Delta\rho g,$$

and the speed of Darcyian flow through the unperturbed matrix

$$c_0 = k_0\Delta\rho g/\left(\mu_f\phi_0\right) \tag{16}$$

[12] Making use of these scales, the nondimensional forms of equations (10) and (11) are

$$\frac{\partial f}{\partial t_c} = (1 - \phi_0 f)f^m\frac{p}{1 - H(p)(1 - R)} - v_s'\nabla f \tag{17}$$

$$f^m\frac{p}{1 - H(p)(1 - R)} = \nabla \cdot \{f^n[\nabla p - (1 - \phi_0 f)u_z]\} \tag{18}$$

where $f = \phi/\phi_0$ is the dimensionless porosity, $p = -p_e/p^*$ is the dimensionless fluid overpressure relative to lithostatic conditions, $v'_s = v_s/c_0$ is the dimensionless matrix velocity, and $t_c = t/t^*$ is the dimensionless time defined relative to the characteristic compaction time

$$t^* = \delta/c_0 \tag{19}$$

[13] A consequence of the asymmetric viscous rheology is that decompaction occurs on scales dictated by the effective viscosity for decompaction, rather than the viscosity for compaction. The decompaction scales for length, time, and pressure can be expressed as a function of R as

$$\delta_d = \delta\sqrt{R}$$
$$t_d^* = t^*\sqrt{R}$$
$$p_d^* = p^*\sqrt{R} \tag{20}$$

[14] For dimensional argumentation we take the parameter values listed in Table 1 as order of magnitude estimates for the scales of asthenospheric melt flow. The influence of the effective decompaction viscosity is explored via R, which is taken as a free parameter in the range 10^0-10^{-6}.

[15] To demonstrate that the porosity advection term in equation (17) is negligible in the small porosity limit $(1 - \phi) \to 1$, we consider one-dimensional compaction, a simplification justified by the expectation gleaned from symmetric viscous compaction models that in higher dimensions the divergence of the matrix velocity is greatest in the direction of fluid expulsion [Scott, 1988; Barcilon and Lovera, 1989; Wiggins and Spiegelman, 1995]. For a compacting region (i.e., $p < 0$), equation (17) is then

$$\frac{\partial f}{\partial t_c} = (1 - \phi_0 f) f^m p - v'_s \frac{\partial f}{\partial z'} \qquad (21)$$

[16] Adopting a barycentric coordinate frame, equation (7) gives the dimensionless matrix velocity v'_s relative to that of the fluid $v'_f = v_f/c_0$ as

$$v'_s = -f v'_f/(1/\phi_0 - f) \qquad (22)$$

from which it is apparent that if all other factors are of $O(1)$ as expected by from the choice of scales, then in the small porosity limit the porosity advection term will be of $O(\phi_0)$ and can be neglected. If equations (17) and (18) are reformulated in terms the length, time and pressure scales for decompaction (equation (20)) the same result is obtained for a decompacting region. Accordingly, we drop the advective term from equation (17) and explicitly introduce the small porosity approximation $1 - \phi \approx 1$ in equations (17) and (18) to obtain

$$\frac{\partial f}{\partial t_c} = f^m \frac{p}{1 - H(p)(1 - R)} \qquad (23)$$

$$f^m \frac{p}{1 - H(p)(1 - R)} = \nabla \cdot [f^n (\nabla p - u_z)] \qquad (24)$$

[17] Equations (23) and (24) then form a closed system of equations in $\{f, p\}$ that we solve numerically. A consequence of the small porosity approximation is that equations (23) and (24) are insensitive to the physical constraint $\phi < 1$ with the further consequence that the amplitudes of steady state porosity waves in a viscous matrix are an increasing function of wave speed [Barcilon and Lovera, 1989; Barcilon and Richter, 1986]. Thus there is no question that there are solutions to equations (23) and (24) for which the porosity would become large enough to cause disaggregation, the issue to be addressed here is whether transient effects may permit such solutions to develop from small flow perturbations.

[18] To clarify the physical implications of our approximate formulation, we remark that equation (3) admits two limiting modes of fluid transport [Scott and Stevenson, 1986]. If the advective term dominates, fluid movement relative to the matrix is insignificant and fluid migration occurs by diapiric upwelling due to the buoyancy of a region of elevated porosity. This phenomenon has been studied extensively without consideration of the dilational term. These studies have shown that for asthenospheric conditions, rates of diapiric upwelling [Weinberg and Podladchikov, 1995; Hall and Kincaid, 2001] achieve maximum velocities of $O(10)$ m yr^{-1}. Here we isolate the alternative limiting mode of transport admitted by equation (5), in which a pulse of porosity is propagated through the matrix, i.e., the porosity wave end-member. In this case the dilational term is essential to describing the phenomenon, but the integrated effect of the advective term is negligible for small porosity problems as the total displacement of the matrix due to expulsion of the fluid is small. Indeed, the advective term has minor influence on steady state viscous compaction profiles with porosity variations as large as 25% [e.g., Connolly and Podladchikov, 2000].

2.2. Relationship Between Wave Speed and Amplitude

[19] The relationship between the speed (c) and amplitude of a porosity wave is essential to assessing waves as a potential transport mechanism. In this regard, the porosity dependence of the bulk viscosity (equation (12)) is critical [Connolly and Podladchikov, 1998]. Analytical treatments that assume no porosity dependence give a linear relationship $\omega = 2A + 1$ ($n = 3$, $m = 0$) for one-dimensional solitary waves [Barcilon and Richter, 1986], where ω is the dimensionless speed (c/c_0) and the amplitude A is taken as the maximum dimensionless porosity. Following the approach outlined by Barcilon and Richter [1986], the speed-amplitude relation derived for the present formulation ($n = 3$, $m = 1$) is

$$\omega = 3 - \frac{4 - 9A + [5 - 6\ln(A)]A^3}{(1 - A)^2(A + 2)} \qquad (25)$$

[20] In the limit of large ($A > 10$) amplitude waves, equation (25) simplifies to a logarithmic relationship between speed and amplitude

$$\omega \approx 6 \ln A \qquad (26)$$

which will be shown to be relevant here. This strong dependence of amplitude on speed implies only a limited range of transport speeds can be achieved without causing the matrix to disaggregate to a magmatic suspension.

2.3. Numerical Methods

[21] Equations (23) and (24) are solved by a second-order alternating direction finite difference scheme. In the direction of implicit solution, equation (24) is used to compute p at time level $q + 1$ from the estimated value of f at the same time level. The estimate of f is then recomputed from its value at time level q and equation (23). This procedure is repeated until the relative change between successive estimates of f is less than an arbitrary tolerance (10^{-12}). The horizontal boundary conditions are $p = 0$, and mirror symmetry is applied for the vertical boundaries.

[22] Convergence tests and comparison of numerical solutions with one- and two-dimensional analytical solutions for viscous formulations indicate that a minimum of eight nodes per compaction length is necessary to accurately resolve flow instabilities. The differing length scales for
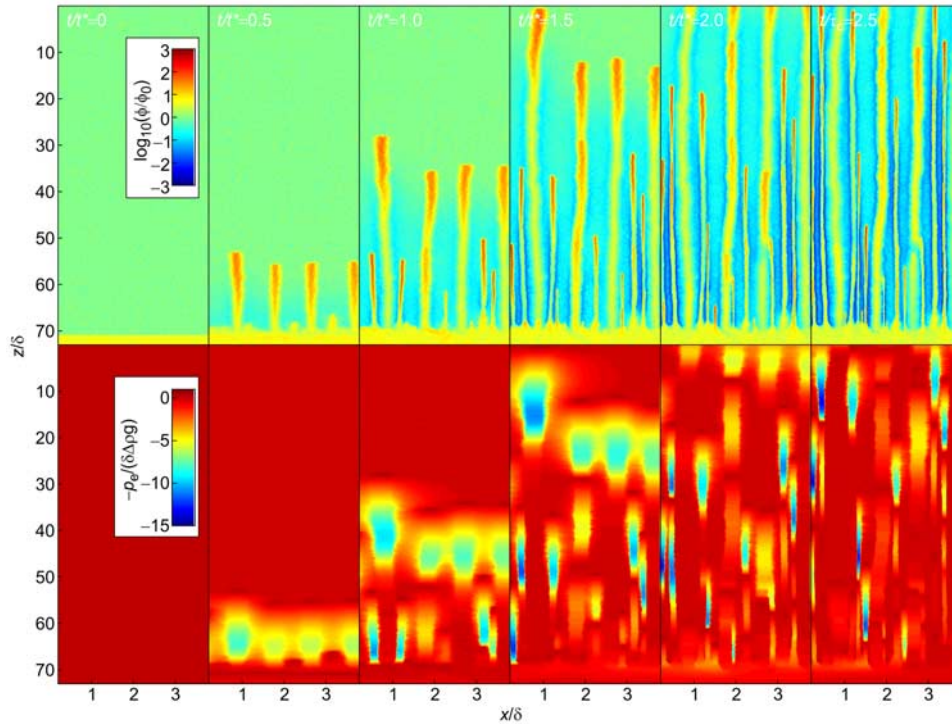
Figure 2. Two-dimensional numerical simulation of fluid flow through a matrix with decompaction weakening ($R = 10^{-3}$) as it evolves from a 60 δ thick layer with elevated porosity bounded from above and below by regions with an order of magnitude lower porosity. (top) Porosity in the uppermost portion of the layer and in the overlying region; (bottom) corresponding distribution of fluid overpressure. Initial waves ($t_c = 0.5$) form with characteristic spacing identical to the viscous compaction length and leave a trail of slightly elevated porosity, flanked by fluid depleted matrix. Depletion of the matrix reduces the local compaction length scale for the initiation of subsequent waves ($t_c = 1$). These waves collect within the trails of the initial waves, so that at $30-40$ δ from the initial obstruction, flow is again channelized on the length scale δ. By analogy with the three-dimensional viscous case [*Wiggins and Spiegelman*, 1995], it is presumed here that the three-dimensional expression of the channels would be pipe-like structures, a presumption recently validated by three-dimensional numerical models (B. J. P. Kaus, personal communication, 2006).

compaction and decompaction creates practical difficulties that we circumvent by two distinct strategies. To model multiple flow instabilities simultaneously, we employ a grid with lateral and vertical spacing proportional to δ_d and δ, respectively. This approach accurately resolves flow channeling, but overestimates the velocity of channel propagation by as much as a factor of two because the vertical grid spacing is inadequate to resolve the shape of overpressured regions. To accurately resolve all features of an isolated instability over long periods of model time, we employ a variable spaced grid that is propagated vertically together with the flow instability. In the vertical direction, the grid is divided into three regions; in the uppermost and lowermost regions the grid spacing is constant and proportional to δ, whereas in the central region the grid spacing is constant and proportional to δ_d. The grid is propagated periodically so that the point within the instability at which f is a maximum remains near the lower boundary of the central region. The propagation is done when the instability has moved a distance corresponding to the nodal spacing of the low-resolution region. The values of p for the solution

at the high-resolution nodes created by grid propagation are obtained by linear interpolation, whereas f at the low-resolution nodes created by grid propagation is adjusted to conserve the porosity that was previously present within the intervening high-resolution nodes.

3. Flow Channelization From a Large Source

[23] We begin by considering fluid expulsion from a large (i.e., vertical and lateral extent $\gg \delta$) region of elevated porosity obstructed from above by a region of low porosity ($t = 0$, Figure 2). For this configuration, numerical simulation demonstrates that the obstruction induces strongly channeled fluid flow. The channels are propagated by porosity waves of extraordinary amplitude and speed that leave a trail of incompletely compacted porosity in their wake. These trails act as preferential pathways for subsequent waves, and develop initially with spacing comparable to δ and width comparable to δ_d, a result suggesting that these scales are appropriate for the channelization process. The waves are propagated by a small region of overpressure

that decompacts the matrix (Figure 2). A much large region of under pressure beneath the overpressured region is necessary for compaction to expel the fluid required to fill the porosity created by decompaction. As compaction occurs on the scale of δ and decompaction on the scale of δ_d, the passage of the waves causes a reduction of the background porosity with the consequence that the waves must gain fluid as they propagate. The reduction in porosity caused by the passage of the initial wavefront reduces the local compaction length for subsequent waves that nucleate between the initial channels. This effect causes channelization above the initial flow obstruction to occur on progressively finer scales with time. However, the net effect of interactions between waves developed on different length scales is to focus the waves into the channels left by the initial wavefront, so that by the time secondary waves have propagated $30-40$ δ most flow is confined within the primary channels.

[24] Because the volume carried by porosity waves may be much less than that of the source region, it is to be expected the area of a "large" source region has little influence on the waves that form from it. Numerical experiments conducted to quantify the spatial domain that qualifies as large with the decompaction weakening rheology show that it is surprisingly small, $\sim 10-100$ δ^2 $\sqrt{R}$. Thus a numerical experiment for a configuration as just discussed (Figure 2), but with a layer thickness of $\delta/2$, initially yields essentially identical waves. However, because the initial wavefront removes a large fraction of the source volume, waves that nucleate later in the experiment are significantly smaller.

[25] Three-dimensional models of compaction-driven fluid flow show that porosity waves in a viscous matrix develop with radial symmetry orthogonal to the direction of propagation [*Wiggins and Spiegelman*, 1995]. As decompaction weakening introduces no inherent asymmetry orthogonal to the direction of flow, we infer that the channels in our two-dimensional simulations develop with radial symmetry in three dimensions, i.e., as pipe-like structures, and inference validated by recent three-dimensional models (B. J. P. Kaus, personal communication, 2006). Thus, in natural settings, the channels would focus pervasive fluxes by a factor of $\sim 1/R$. In natural settings, the most probable effect of far-field tectonic stresses would to flatten the channels into more dike-like structures, in which case the focusing factor would approach $\sim 1/\sqrt{R}$.

4. Wave Evolution From Small Sources: Return of the Blob

[26] The dynamics of solitary wave nucleation are such that even for the symmetric viscous case there is no simple relation between the excess volume of the source and that of waves which evolve from it, where excess volume is the amount of porosity above the background level integrated over the source region, i.e., fluid volume in excess of that contained by the background porosity. There is, however, a monotonic relationship between wave excess volume and speed. While the details of this relationship vary depending on geometry and constitutive relations [*Barcilon and Richter*, 1986; *Barcilon and Lovera*, 1989; *Wiggins and Spiegelman*, 1995; *Connolly and Podladchikov*, 1998],

excess volume approaches zero monotonically as the dimensionless speed (ω) drops below the porosity exponent n in the permeability function [*Connolly and Podladchikov*, 1998]. Thus to provide a scale, albeit arbitrarily, to define small excess volumes we observe that the excess volume of the viscous solution for $\omega = 3$ is $\sim 10^3$ (a result obtained by taking the one-dimensional analytical solution as a proxy for the three-dimensional case as described later). Thus a large volume of fluid is necessary to nucleate a solitary wave with a speed slightly above the minimum at which the wave is stable, e.g., if the spatial extent of the source region is δ^3, then the fluid fraction in this source region necessary to nucleate a wave is $\sim 10^3$ ϕ_0. While the observation that the solitary waves in a viscous matrix do not lose mass as they propagate was thought to make them an effective transport mechanism [*Scott and Stevenson*, 1984; *Richter and McKenzie*, 1984] the corollary that they cannot gain mass in combination with the requirement of a large source excess porosity suggests they are ineffective for extracting small quantities of melt. In contrast, the depletion of the background porosity observed with decompaction weakening (Figure 2) suggests that the waves gain mass as they propagate. Anticipating that this imbalance influences transient dynamics so as to allow solitary waves to nucleate from minute perturbations in a decompaction weakening matrix we proceed to investigate this scenario.

[27] The magnitude of the source porosity relative to the background level has important influence on wave generation, such that low-amplitude sources generate low-amplitude (speed) waves or may even hinder nucleation. However, our concern is the extraction of melt generated by low degrees of partial melting. In this context, small variations in melt production are sufficient to generate large relative porosities. Thus we focus on the constraint on the excess volume for initial configurations with a maximum relative porosity of two. To resolve wave evolution with decompaction, weakening rheology a series of numerical experiments were undertaken as a function of the parameter R in which waves were nucleated from a circular region of elevated porosity in otherwise uniform background porosity. The initial radial porosity distribution within the circular region was Gaussian with

$$f = 1 + \exp\left[-(r/\lambda)^2\right] \tag{27}$$

where the size parameter λ and resulting excess volume were specified as in Table 2. For this distribution, in both two and three dimensions, essentially all the excess volume of the source region occurs within a radius of $<3\lambda$. Thus, if the viscous compaction length is ~ 1 km, then the initial conditions correspond to a source region with a melt fraction less than twice the background level and spatial dimensions of $10-100$ m. The experiments show that decompaction weakening permits solitary waves to nucleate from sources that are miniscule ($\sim 10^{-2}-10^{-4}$ $\phi_0\delta^3$, Table 2) in comparison to that required for the viscous case ($\sim 10^3$ $\phi_0\delta^3$); but waves did not nucleate in all the experiments (5a and 6a, Table 2). This observation indicates that uniform compaction driven fluid flow through a matrix with decompaction weakening is not inherently unstable. No systematic effort was made to delimit the conditions at

Table 2. Initial Conditions for Numerical Models of Wave Evolution From a Small Source as a Function of R^a

Model	R	λ	F_{2D}	F_{3D}	Wave
1	6.4×10^{-3}	0.16	1.7×10^{-1}	7.1×10^{-2}	yes
2	1.6×10^{-3}	8.2×10^{-1}	4.3×10^{-2}	8.8×10^{-3}	yes
3	4.0×10^{-4}	4.1×10^{-2}	1.1×10^{-2}	1.1×10^{-3}	yes
4	1.0×10^{-4}	2.1×10^{-2}	2.7×10^{-3}	1.4×10^{-4}	yes
5a	2.5×10^{-5}	1.0×10^{-2}	6.7×10^{-4}	1.7×10^{-5}	no
5	2.5×10^{-5}	4.1×10^{-2}	1.1×10^{-2}	1.1×10^{-3}	yes
6a	6.3×10^{-6}	5.2×10^{-3}	1.7×10^{-4}	2.2×10^{-6}	no
6	6.3×10^{-6}	2.1×10^{-2}	2.7×10^{-3}	1.4×10^{-4}	yes

^{a}The spatial extent of the source region is measured by λ (equation (27)); F_{2D} (equation (29)) is the two-dimensional excess volume of the source region; and F_{3D} (equation (28)) is the corresponding three-dimensional excess volume, the last column indicates whether a traveling wave nucleated from the source.

which solitary waves do not nucleate since these conditions must depend on the geometry, extent and amplitude of the flow perturbation.

[28] In the numerical experiments wave evolution occurs in two stages that are best understood from transverse sections through the spatial domain of the models (Figure 3). In the initial stage, the perturbation is propagated upward as a porosity shock ($t_c < 2$, Figure 3). During this stage the divergence of the vertical fluid flux, due to lateral compaction, required for growth of the shock can be maintained by increasing the effective pressure with depth. The maximum effective pressure gradient is limited by hydrostatic fluid pressure, thus the shock becomes unstable once such conditions are achieved. Thereafter a pressure minimum propagates upward from the base of the initial obstruction and the increase in pressure beneath this minimum causes the lower portion of the shock to stagnate.

[29] Separation of the stagnant and dynamic portions of the shock initiates the second stage of wave evolution, whereby the dynamic portion of the shock (Figure 4) is identified as the solitary traveling wave responsible for the channeling instability (Figure 2) discussed previously. This stage is reminiscent of the solitary waves known for the viscous case in that the porosity created by decompaction in the upper part of the wave is restored by compaction at depth. In the viscous case, the pressure anomalies responsible for decompaction and compaction are antisymmetric (Figure 4b) and therefore it is not surprising that the waves evolve toward a steady state in which the background porosity is restored after the wave passage. In detail, numerical simulations show that this restoration is imperfect, so that the waves leave trails of elevated porosity that causes them to lose mass with time, albeit almost imperceptibly. With decompaction weakening the wave wake has a more complex structure (Figure 4a) consisting of a tail of elevated porosity (i.e., $f > 1$), flanked by troughs formed by drainage. Within the resolution of the numerical calculations the effective pressure within the wake vanishes, so the wake is a structure that persists on a long timescale.

4.1. Speed and Amplitude

[30] A remarkable feature of decompaction weakening solitary wave solutions with is that they have virtually identical speed-amplitude relationships, which are, in turn, nearly identical to that of the symmetric viscous solution

(Figure 5a). Early work on solitary wave solutions in viscous media emphasized distinctions between one-dimensional and multidimensional solutions that are important for the small amplitude waves that initiate in the viscous scenario [*Barcilon and Richter*, 1986; *Barcilon and Lovera*, 1989]. The simulations here demonstrate that extraordinary amplitudes may be achieved by waves in a decompaction weakening matrix. For such large amplitude waves the distinction between one-dimensional and multidimensional solutions becomes insignificant [*Barcilon and Lovera*, 1989]. Thus the logarithmic speed-amplitude relationship (equation (25)) predicted for the one-dimensional steady state is essentially that which is observed in the numerical simulations.

4.2. Rescaling to the Viscous Steady State

[31] The similarity in speed-amplitude relationships indicates that the solitary waves that develop with decompaction weakening correspond to a quasi-steady state that is closely related to symmetric viscous steady state in which the waves propagate with constant speed and unchanging form. The origin of this similarity is that waves are propagated by decompaction, which occurs on a much
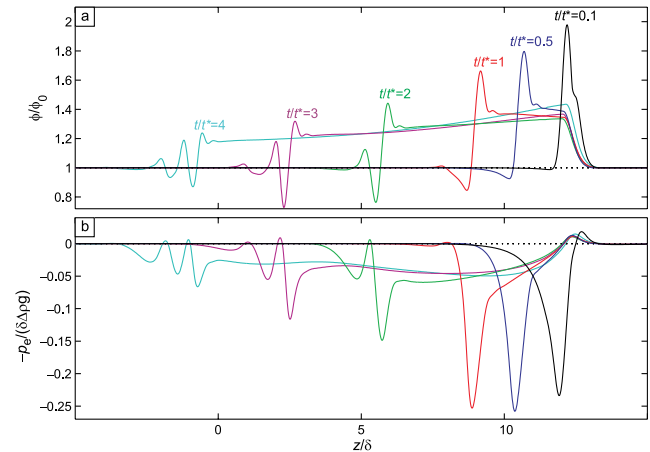

Figure 3. Vertical profiles of porosity and pressure from a two-dimensional model with a Gaussian initial porosity distribution (equation (27), $R = 6.4 \times 10^{-3}$, model 1, Table 2). Absolute profile coordinates are arbitrary; that is, profiles are positioned so that the maximum pressure for each profile approximately coincides. The porosity profile time labels are positioned over the initial source region. At $t_c = 0.1$, the initial porosity profile has a small shoulder corresponding to the nascent shock, and shock amplitude initially decays as the front propagates away form its source ($t_c = 0.5-1$). At $t_c \sim 2$ this trend reverses, and the shock amplitude begins to grow coincidentally with separation of a broad pressure minimum from the source region. Separation of this minimum, coupled with the superjacent pressure maximum, initiates the quasi-steady state phase of the wave. Thereafter, the relationship between wave amplitude and speed is essentially identical to that for the symmetric viscous steady state (equation (25), Figure 5). Increased porosity in the vertical profiles is generated by compaction of the matrix orthogonal to the flow direction (Figure 4).
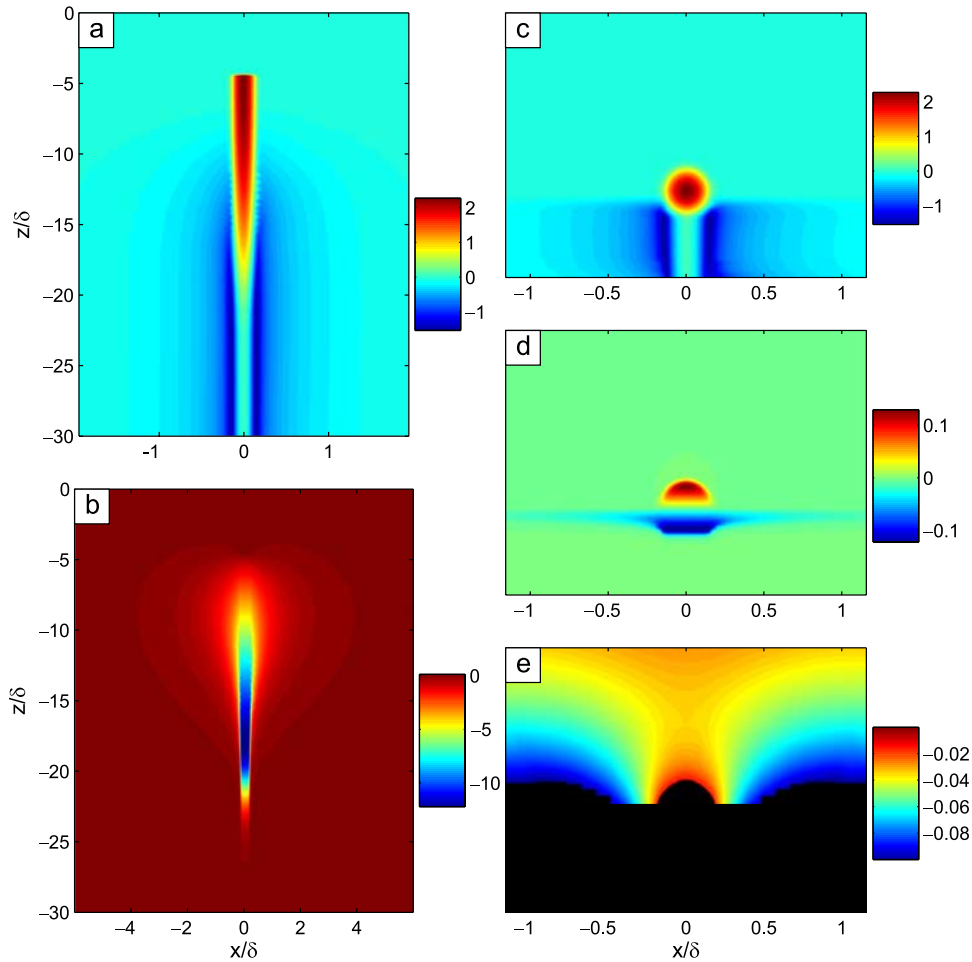
Figure 4. Two-dimensional (a) ($\log_{10}$) porosity and (b) pressure distributions (with different lateral scales) associated with a solitary porosity wave in a matrix with decompaction weakening ($R = 10^{-3}$, $t_c = 9.5$). Depletion of the porosity on either side of the wave tail is caused by the imbalance in fluid circulation resulting from the asymmetric pressure distribution. (c) The radially symmetric porosity distribution of the viscous solitary wave solution is recovered from the porosity distribution by stretching the compacting region by a factor of $\sqrt{R}$ (the lateral asymmetry in this image due to the graphics rendering program and not present in the primary data). (d) Application of the same transformation to the pressure distribution shows that while the absolute value of the transformed pressure minimum is essentially identical to that of the pressure maximum, the pressure distribution is distorted from the antisymmetric dipolar field characteristic of the viscous solution [*Scott and Stevenson*, 1986; *Barcilon and Lovera*, 1989]. (e) Detail of pressure (in the range 0 to -0.1) above the equator of the transformed porosity distribution which shows that the decompacting region is enveloped by the compactive pressure field induced by fluid drainage at greater depth.

shorter timescale than compaction if $R \ll 1$. Thus the decompacting region evolves toward a steady state that is essentially independent of the compaction process at greater depth and therefore identical to the upper hemisphere of the symmetric viscous stationary solution with $\zeta = \zeta_c R$ and length scale $\delta_d = \delta\sqrt{R}$ (Figure 6). In contrast, in the compacting region the operative length scale is δ; thus porosity generated by decompaction is restored on this longer length scale. The increased length scale for compaction causes the restoration to be stretched in the direction of propagation resulting in a semiellipse of elevated porosity beneath the decompacting region. This argumentation suggests that the porosity distribution in the compacting region can be transformed to that of the viscous solution by scaling the vertical coordinate by $\sqrt{R}$. Application of this transformation to the numerical results does indeed recover a close approximation of the radially symmetric porosity distribution of the viscous steady state (Figure 4c). For $R \ll 1$, the excess volume in the decompacting portion of the wave is insignificant; thus the transformation implies $F/\sqrt{R}$ must be approximately half the excess volume of the viscous steady state, as is demonstrably the case in the numerical models (Figure 5b).

[32] The stretching transformation cannot recover the dipolar pressure field of the symmetric viscous steady state because fluid underpressure associated with compaction
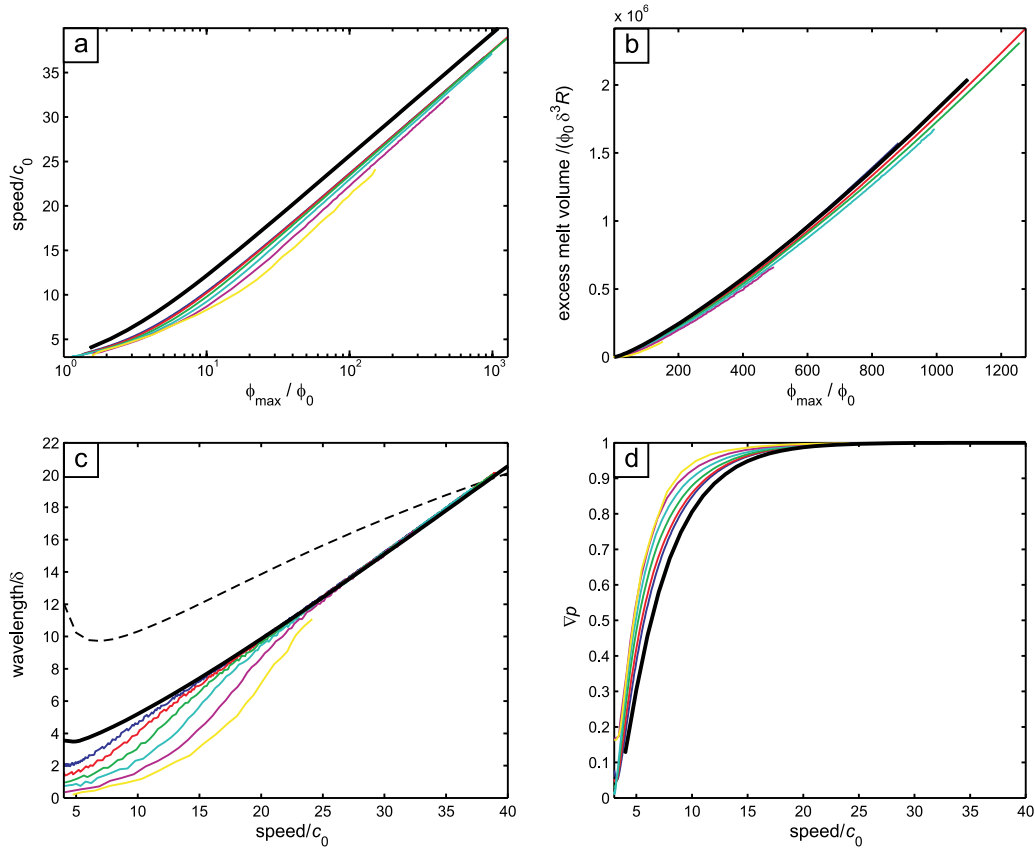
Figure 5. Wave properties as a function of R (dark blue, 6.4×10^{-3}; red, 1.6×10^{-3}; green, 4.0×10^{-4}; light blue, 1.0×10^{-4}; magenta, 2.5×10^{-5}; yellow, 6.3×10^{-6}) compared to properties derived from the analytical one-dimensional solitary wave solution (black curves) for the symmetric viscous case. (a) Logarithmic relationship between amplitude and speed obtained for the present formulation (equation (26)) which has implications for melt transport because it allows only a limited range of wave speeds as compared to the linear relation derived in studies that neglect the porosity dependence of the bulk viscosity. (b) Three-dimensional excess volume scaled by R as a function of amplitude. Three-dimensional volumes are obtained from two- and one-dimensional numerical and analytical solutions as discussed in the text. (c) Wavelength, measured by the distance from the porosity maximum to the pressure minimum, as a function of speed, >98% of the excess volume associated with a wave occurs over this interval. The dashed curve is twice the second moment of the porosity distribution obtained for the one-dimensional analytical solution. (d) Pressure gradient at the porosity maximum as a function of speed. That numerical results deviate from the analytical solution most strongly at low speeds is expected in that at low speeds both wave size and pressure gradient vary, whereas at higher speeds the variation in pressure gradient becomes insignificant.

develops around the compacting region on the scale δ (Figure 4d). The underpressure induces compaction and drainage of portions of the matrix that have not been perturbed by decompaction (Figures 4a and 6), a pattern that results in the imbalance in fluid circulation responsible for wave growth. In detail, the greater length scale for fluid underpressure causes the decompacting region to be enveloped by underpressure induced by compaction at depth (Figures 4e and 6). This phenomenon has the peculiar consequence that the matrix may compact in advance of the dilational portion of the waves and explains the slight differences in the speed-amplitude relations, in that as R decreases, larger amplitudes are required to achieve a given speed.

[33] The size of solitary wave is equivocal because the steady state porosity distribution asymptotically approaches the background porosity. However, because the distribution is nearly Gaussian, >99% of porosity occurs within twice the second moment of the porosity distribution λ_ϕ. Unfortunately, λ_ϕ was not recovered from the numerical calculations; therefore we use the distance between the porosity and pressure maxima λ_p as a measure of wave size in the vertical direction; one-dimensional analytical solutions for λ_ϕ and λ_p indicate that these measures differ by less than a factor of two (Figure 5c). For large waves in a decompaction weakening matrix λ_p converges to the one-dimensional viscous steady state, but for small waves there is a marked dependence of λ_p on R. This dependence is
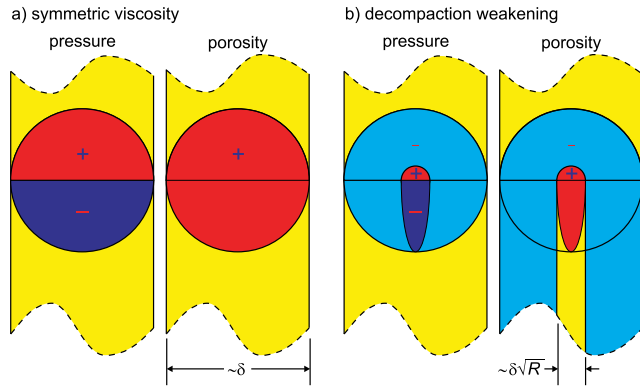
Figure 6. Illustration of the scaling arguments used to relate the solitary wave solution in (a) the symmetric viscous case to (b) the solitary waves that develop in a matrix with decompaction weakening. Yellow indicates background values of pressure and porosity, red indicates elevated values, and light and dark blue indicate weakly and strongly depressed, respectively, values. In the symmetric viscous case, the pressure distribution associated with a porosity wave is an antisymmetric dipole so that fluid circulation is perfectly balanced and the wave has no tendency to gain or lose mass. With decompaction weakening, fluid underpressures and compaction develop on the length scale δ as in the symmetric viscous case, whereas decompaction and overpressure develop on the shorter length scale $\delta\sqrt{R}$. Thus decompaction generates an elevated region of porosity and pressure analogous to the upper hemisphere of the symmetric viscous case but on this shorter length scale. Restoration of this elevated porosity occurs on the length scale δ, which causes the compacting portion of the wave to develop a semiellipsoidal geometry. Fluid underpressure in the compacting region relaxes on the length scale δ, causing compaction of the matrix in advance of the wave as well as in laterally adjacent portions of the matrix that have not been perturbed by decompaction.

attributed to the fact that in small waves the pressure gradient varies as a function of amplitude, whereas in large waves the pressure gradient is effectively constant.

[34] To estimate the three-dimensional excess volumes that correspond to our two-dimensional numerical solutions, we observe that radial porosity distribution for the two-dimensional viscous steady state [*Barcilon and Lovera*, 1989] differs insignificantly from the one-dimensional steady state [*Barcilon and Richter*, 1986]. Under the assumption that the three-dimensional porosity distribution is likewise the spherically symmetric equivalent of the two-dimensional case [cf. *Wiggins and Spiegelman*, 1995], the excess volume of the viscous steady state

$$F = \pi \int_0^\infty (2r)^{d-1}(f-1)\,dr \qquad (28)$$

where d is the dimension of the solution, is approximated by substituting the one-dimensional porosity distribution ($n = 3$, $m = 1$) for f. Comparison of this integration yields an

empirical function relating the volume of the three-dimensional viscous steady state to that of the two-dimensional case

$$F_{3D} = \sum_{i=1}^{3} b_i F_{2D}^i \qquad (29)$$

for $F_{2D} = 0 \rightarrow 3.4 \times 10^5$ with $\{b_1 = 13.1, b_2 = 1.70 \times 10^{-5}, b_2 = -2.53 \times 10^{-11}\}$. Given that the stretching transformation (i.e., $z' = z\sqrt{R}$) of the compacting region for waves developed under decompaction weakening recovers the radial symmetry of the symmetric viscous solution (Figures 4b and 5c), it follows that the three-dimensional excess volumes for the decompaction weakening rheology can be expressed from equation (29) as

$$F = R\sum_{i=1}^{3} b_i \left(F_{2D}/\sqrt{R}\right)^i \qquad (30)$$

[35] Making use of λ_p as a measure of wave size, the volume of matrix affected by a solitary wave is

$$V \approx \frac{2}{3}\pi\lambda_p^3 R \qquad (31)$$

and the average excess porosity within a wave is
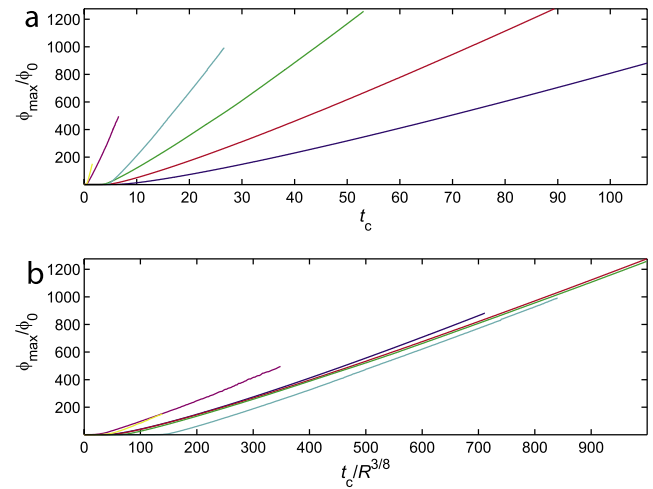
$$f_{avg} = \frac{F}{V} \qquad (32)$$

Figure 7. Wave amplitude as a function (a) of time and (b) of the rescaled time variable $t_c R^{-3/8}$. Colors indicate the value of R as in Figure 5. Porosity evolution prior to initiation of quasi-steady state (Figure 3) is dependent on the geometry of the initial perturbation, which varied in the numerical experiments. Because wave amplitude varies little in this initial phase, the curves appear to intercept the time axis at $t_c > 1$. In the limit that wave growth is truly self-similar in time, with scaling as $t_c R^{-3/8}$, the rescaled curves should have the identical slopes as a function of amplitude after achievement of the quasi-steady state.
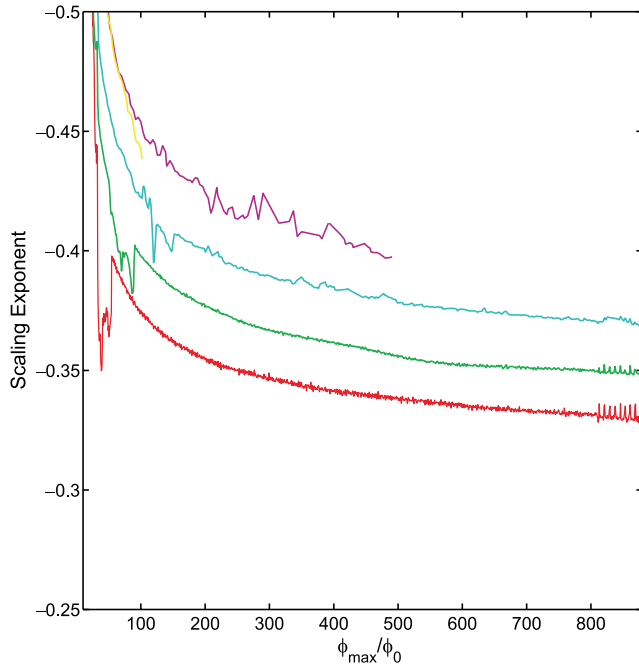
Figure 8. Value of the scaling exponent as a function of wave amplitude obtained by equating the wave growth rates for the numerical simulation with $R = 6.4 \times 10^{-3}$ to those obtained for $R = 1.6 \times 10^{-3}$ (red), $R = 4.0 \times 10^{-4}$ (green), $R = 10^{-4}$ (light blue), $R = 2.5 \times 10^{-5}$ (magenta), and $R = 6.3 \times 10^{-6}$ (yellow). A value of $-1/2$, as observed in the initial stages of wave growth, indicates the compaction timescale is determined entirely by the effective bulk viscosity in decompaction. At larger amplitudes, the scaling exponent varies by ± 0.05 around the value of $-3/8$ taken here to obtain a growth function (equation (36)). Although there is no distinct break in the dependence of the scaling exponent on amplitude, the weaker dependence observed for large amplitudes does correlate with the conditions at which the maximum pressure gradient within the waves ceases to vary significantly ($\omega \sim 20$, $A \sim 100$, Figures 5a and 5d).

which evaluates to $\sim 0.2\,A$ for $A = 100 - 1000$.

4.3. Growth

[36] The growth rate of quasi-steady state solitary waves varies as a strong function of R (Figure 7a), but to the extent that the steady state is a valid approximation it is to be expected that transient wave evolution is self-similar. In this case it should be possible to scale time by a function of R to obtain a universal growth rate function. For this purpose we assume a power function R^x, so that scaled time variable becomes $t_c R^x$, and solve for the unknown exponent x by equating the scaled growth rates for excess volume, $(R^{-x}/F)(\partial F/\partial t_c)$, for numerical simulations at different R values (Figure 8). This exercise give values for x between $-1/2$ and $-1/4$, suggesting that compared to the compaction timescale ($x = 0$), the timescale for decompaction ($x = -1/2$) dominates growth rates. To a first approximation, scaling with $x = -3/8$ is adequate to represent the numerical results (Figure 7b), implying that wave amplitude can be expressed as a linear function of time for $10^{-2} > R > 10^{-6}$. Using this

function, a first-order accurate parameterization of the numerical results for $A > 10$ yields

$$A \approx t_c / R^{3/8} \tag{33}$$

$$\omega \approx 6 \ln A - 4 \tag{34}$$

$$F \approx 1850 A R \tag{35}$$

$$\lambda_p \approx \omega / 2 \tag{36}$$

[37] This parameterization provides a number of useful results, among these are that waves propagate a distance comparable to their own wavelength in a dimensional time of $t^*/2$ (equation (36)) and that the time required for a wave to disaggregate the matrix (i.e., $A = \phi_d/\phi_0$) is $t^* R^{3/8}\,\phi_d/\phi_0$ (equation (33)). The discrepancy between the velocity of a solitary wave and that of the background fluid flux gives rise to a net flux through the solitary wave with the result that the fluid generally travels more slowly than the porosity [*Richter and McKenzie*, 1984; *Scott and Stevenson*, 1986]. Thus while the volume carried by the wave is of magnitude ωF, the excess fluid flux is of magnitude $\omega(F - 1)$, a distinction that is insignificant for large amplitude waves.

4.4. Dissipation

[38] Porosity waves must dissipate gravitational potential energy as heat. In dimensional form, the volumetrically averaged buoyancy force acting on the wave is $\phi_0 f_{avg} \Delta \rho g$, thus the power per unit volume generated by dissipation is

$$P = \phi_0 f_{avg} \Delta \rho g \omega c_0 \tag{37}$$

which is independent of R, but varies as $\sim 5A$ from equations (32) and (34)–(36). If neither melting nor freezing occurs and heating is confined to the wave channel of radius $\delta \lambda_p \sqrt{R}$, the temperature increase in the channel caused by the passage of the wave is

$$\Delta T = \frac{\delta}{c_0} \frac{P}{C_p} \tag{38}$$

[39] Making use of equations (31), (33), and (35), with $A = 0.2/\phi_0$ as an upper limit on amplitude and the parameter ranges in Table 1, equation (38) indicates the temperature change caused by the passage of a large wave is $1 - 10$ K. Such a thermal effects might weaken the matrix and thereby generate a positive feedback that further enhances channelized flow. An alternative limiting scenario is that the matrix is at eutectic conditions, in which case the power generated by dissipation is consumed by melting. The dimensional melting rate is then

$$\Gamma^{\text{melting}} = \frac{1}{\phi_0 f_{avg}} \frac{P}{L} \tag{39}$$

where L is the latent heat of melting. To assess the potential importance of dissipation induced melting, Γ^{melting} can be

compared to wave growth rates ($1/F\,(\partial F/\partial t_c)$, from equation (35)) due solely to decompaction weakening

$$\Gamma^{\text{mech}} = \frac{c_0}{\delta}\,\frac{1}{AR^{3/8}} \qquad (40)$$

[40] The rates Γ^{melting} and Γ^{mech} correlate inversely with amplitude, thus wave growth due to dissipation induced melting becomes more important in large amplitude waves. For asthenospheric parameter ranges (Table 1) and $A = 0.2/\phi_0$, the two rates are equal at values of R between 10^{-2} and 10^{-4}. A result suggesting that dissipative heating has the potential to significantly enhance growth rates.

5. Prediction of Wave Properties From a Large Source

[41] Porosity waves are a mechanism by which a fluid flux in excess of the flux that can pass through the unperturbed background porosity is accommodated in deformable porous media. While there is no strict relation between the flux carried by waves and that of a source, numerical models of fluid expulsion from large volume sources [*Spiegelman*, 1993; *Connolly and Podladchikov*, 1998], or equivalently a source of high fluid flux, i.e., a fluid producing chemical reaction [*Connolly*, 1997], show that the flux carried by waves is comparable to the source flux. Taking proximity to such a steady state as an ansatz, equation (36) provides a basis for predicting the properties of waves that nucleate from a large source. Making use of the observation that such waves form with spacing $\sim\delta$, if the magnitude of the integrated excess flux within the source region is $(q - q_0) \approx q$, then the flux channeled into a wave must be of magnitude $\approx q\pi\delta^2/4$. Equating this flux magnitude to that of the flux carried by a wave ($\approx c_0\phi_0\delta^3\omega F$), with equations (32) and (36), yields

$$q = \frac{14800 R k_0 \phi_{\max}}{\pi \mu \phi_0}\left(3\ln\frac{\phi_{\max}}{\phi_0} - 2\right) \qquad (41)$$

where $\phi_{\max}$ is the maximum porosity of a wave generated from the source. Equation (41) can be rewritten in terms of the source region porosity ϕ_{source}, under the assumption that the source region is initially noncompacting (i.e., $q = k\Delta\rho g/\mu$), as

$$\phi_{\text{source}} = \sqrt[3]{\frac{14800R}{\pi}\phi_{\max}\phi_0^2\left(3\ln\frac{\phi_{\max}}{\phi_0} - 2\right)} \qquad (42)$$

[42] An implication of equation (42) is that the source porosity required to achieve a given maximum porosity is strongly dependent on ϕ_0, e.g., to obtain $\phi_{\max} = 0.2$ with $R = 10^{-3}$, $\phi_{\text{source}}/\phi_0$ varies from 9 to 58 as ϕ_0 varies from 10^{-2} to 10^{-4}. This result depends on $\sqrt[3]{R}$, thus decreasing R by 3 orders of magnitude, lowers $\phi_{\text{source}}/\phi_0$ by only an order of magnitude. Porosity contrasts of greater than 2 orders of magnitude are easily within the range generated by low variance melting and devolatilization reactions [*Connolly*, 1997; *Connolly et al.*, 1997]; thus even weak manifestations

of decompaction weakening in high-grade metamorphic settings may be adequate to cause disaggregation.

6. Discussion

[43] The quantitative features of the results presented here are specific to the formulation, but the model does depict a fundamental consequence of asymmetry in compaction and decompaction. Specifically, it demonstrates that the asymmetry in the pressure field associated with flow instabilities induces unbalanced fluid circulation that causes the instabilities to grow with time. The implications for melt transport are that porosity waves may nucleate from much smaller perturbations, and may grow to much larger amplitudes, than expected on the basis of symmetric viscous compaction models. Thus we conclude that porosity waves are a mechanism capable of bridging the gap between pervasive and segregated melt flow.

[44] The relationship between wave amplitude and speed is critical to evaluating the efficacy of fluid transport by porosity waves and is particularly sensitive to the constitutive law chosen to define the bulk viscosity, ζ. Theory [*Nye*, 1953; *Sumita et al.*, 1996] and both field [*Connolly and Podladchikov*, 2000] and experimental [*Ashby*, 1988; *Renner et al.*, 2003] observations support the contention that $\zeta \propto 1/\phi$, yielding a logarithmic relationship between amplitude and speed (equation (26)). Given the asthenospheric compaction timescale ($t^*(y) \sim 6\sqrt{\mu}/\phi_0$, Table 1), melt extraction at porosities $<10^{-4}$ is unlikely to be of geological importance; the upper limit $O(10^{-1})$ on the porosities of interest here occurs when the matrix disaggregates to a magmatic suspension [*Arzi*, 1978; *Auer et al.*, 1981; *Ashby*, 1988]. Thus, for asthenospheric melt transport, relevant porosity wave amplitudes are <1000, implying that porosity waves have the potential to increase melt transport speeds by a factor of <100 over background flow rates. Adopting parameters appropriate for asthenospheric melting processes (Table 1), these speeds are $\sim 10-100$ m yr^{-1}.

[45] The foregoing speed constraints are derived by exploiting the numerical observation that decompaction weakening does not significantly affect the relationship between wave amplitude and speed. However, wave growth and therefore the time required to achieve a given speed are critically dependent on decompaction weakening, characterized here by the parameter R. In the absence of quantitative experimental or theoretical models, field evidence of asthenospheric melt channelization can be used to infer the R values necessary to explain channelization as a consequence of decompaction weakening. Such evidence in the Kohistan Arc indicates that melts [*Jagoutz et al.*, 2006] have been focused into pipe-like channels of ~ 500 m radius with spacing of ~ 10 km, requiring $R \sim 10^{-2}$. Taking this value for the sake of illustration, consider the segregation of kimberlitic melt ($\mu = 10^{-1}$ Pa s) initially present at a melt fraction $\phi_0 = 10^{-3}$ such as often considered necessary to explain kimberlite geochemistry [*Khazan and Fialko*, 2005]. For this scenario, from equation (32), a flow instability would accumulate 10 km^3 of melt in 6000 years, during which time the instability would propagate 67 km and achieve a speed of 20 m yr^{-1} and a maximum melt fraction of 0.02. Provided that two-dimensional dike models generalize to three dimensions as disk-like structures, this

melt volume is more than adequate to satisfy the geometric constraints imposed by elastic theory for self-propagating dikes [*Fialko and Rubin*, 1999]. Thus we posit that porosity waves are a mechanism of generating the melt reservoir essential to the nucleation of lithospheric dikes. Additionally, because porosity wave propagation causes elevated strain rates, they may provoke the elastic response required to initiate dikes or other high Deborah number transport mechanisms [*Rubin*, 1998; *Phipps Morgan and Holtzman*, 2005].

[46] There is broad agreement that actinide isotopic secular disequilibria observed in mid-ocean ridge (MOR) volcanic rocks require both a pervasive and a localized, more rapid, melt transport mechanism in the subjacent asthenosphere [*McKenzie*, 1985]. In this regard, the reactive infiltration model does not predict transport velocities that are adequate to preserve ^{226}Ra, if this isotope is derived by melting at the base of the asthenosphere. Accordingly, proponents of reactive infiltration argue that ^{226}Ra in MOR volcanics derives from near surface processes [*Kelemen et al.*, 1997; *Spiegelman et al.*, 2001; *Jull et al.*, 2002]. Defense of this argument has been complicated by recent measurements that suggest the fractionations of ^{226}Ra and, its even shorter lived daughter, ^{210}Pb relative to ^{230}Th in MOR basalts are inconsistent with the trends expected from shallow processes and therefore are most easily explained as the signature of incipient melting [*Rubin et al.*, 2005; *Elliott*, 2005], implying transport speeds of $\sim 10^3$ m yr^{-1}. Thus, although decompaction weakening extends the range of transport speeds attainable by porous flow, speeds of this scale exclude porosity waves as the primary mechanism for rapid melt transport beneath mid ocean ridges thereby lending credence to the earlier hypothesis that dikes fulfill this role [*Nicolas*, 1986].

[47] Reactive infiltration and mechanical flow instabilities are mutually reinforcing [*Spiegelman et al.*, 2001], but specific asthenospheric settings may enhance or subdue the role of either mechanism. In this regard it is pertinent to observe that the upper asthenosphere is itself a porosity wave that remains stationary with respect to the earth's surface as the mantle upwells beneath mid-ocean ridges. The uniformity of MOR melt production attests to the existence of a stable mechanical steady state that is likely to limit development of smaller-scale mechanical instabilities such as those discussed here [*Scott and Stevenson*, 1986] but would have little effect on chemical instabilities. In contrast, because the reactive infiltration instability is caused by dissolution of the matrix in the direction of flow it may not operate in the lowermost portion of the asthenosphere where melting is controlled by chemical heterogeneity [*Plank and Langmuir*, 1992; *Hirth and Kohlstedt*, 1996; *Phipps Morgan and Morgan*, 1999]. Likewise, reactive infiltration cannot promote melt flow in hostile environments where transport is hindered by crystallization, notably the upper portion of the mantle wedge, where there is evidence for channelized melt flow with transport speeds of ~ 100 m yr^{-1} [*Turner*, 2002]. Porosity waves generate heat by viscous dissipation (equation (38)) a phenomenon that may favor mechanical instabilities in such settings.

[48] The rheological manifestation of plasticity is favored by falling temperature [*Nicolas and Poirier*, 1976] an effect that should enhance decompaction weakening. A related thermal effect causes the local viscous compaction length to increase upward [*Connolly and Podladchikov*, 1998; *Connolly and Podladchikov*, 2004]. These effects are not incorporated in the numerical models presented here, but we speculate that they cause channelized flows to anastomose upward.

References

Aharonov, E., J. A. Whitehead, P. B. Kelemen, and M. Spiegelman (1995), Channeling instability of upwelling melt in the mantle, *J. Geophys. Res.*, *100*, 20,433–20,450.

Arzi, A. A. (1978), Critical phenomena in rheology of partially melted rocks, *Tectonophysics*, *44*, 173–184.

Ashby, M. F. (1988), The modeling of hot isostatic pressing, in *Proceedings HIP: Hot Isostatic Pressing—Theories and Applications*, edited by T. Garvare, pp. 29–40, Centek, Lulea, Sweden.

Auer, F., H. Berckhemer, and G. Oehlschlegel (1981), Steady-state creep of fine-grain granite at partial melting, *J. Geophys.*, *49*, 89–92.

Barcilon, V., and O. M. Lovera (1989), Solitary waves in magma dynamics, *J. Fluid Mech.*, *204*, 121–133.

Barcilon, V., and F. M. Richter (1986), Nonlinear-waves in compacting media, *J. Fluid Mech.*, *164*, 429–448.

Bercovici, D., Y. Ricard, and G. Schubert (2001), A two-phase model for compaction and damage 1. General theory, *J. Geophys. Res.*, *106*, 8887–8906.

Connolly, J. A. D. (1997), Devolatilization-generated fluid pressure and deformation-propagated fluid flow during prograde regional metamorphism, *J. Geophys. Res.*, *102*, 18,149–18,173.

Connolly, J. A. D., and Y. Y. Podladchikov (1998), Compaction-driven fluid flow in viscoelastic rock, *Geodin. Acta*, *11*, 55–84.

Connolly, J. A. D., and Y. Y. Podladchikov (2000), Temperature-dependent viscoelastic compaction and compartmentalization in sedimentary basins, *Tectonophysics*, *324*, 137–168.

Connolly, J. A. D., and Y. Y. Podladchikov (2004), Fluid flow in compressive tectonic settings: Implications for midcrustal seismic reflectors and downward fluid migration, *J. Geophys. Res.*, *109*, B04201, doi:10.1029/2003JB002822.

Connolly, J. A. D., M. B. Holness, D. C. Rubie, and T. Rushmer (1997), Reaction-induced microcracking: An experimental investigation of a mechanism for enhancing anatectic melt extraction, *Geology*, *25*, 591–594.

Daines, M. J., and D. L. Kohlstedt (1994), The transition from porous to channelized flow due to melt/rock reaction during melt migration, *Geophys. Res. Lett.*, *21*, 145–148.

Elliott, T. (2005), Earth science—Unleaded high-performance, *Nature*, *437*, 485–486.

Fialko, Y. A., and A. M. Rubin (1999), Thermal and mechanical aspects of magma emplacement in giant dike swarms, *J. Geophys. Res.*, *104*, 23,033–23,049.

Forsyth, D. W., et al. (1998), Imaging the deep seismic structure beneath a mid-ocean ridge: The MELT experiment, *Science*, *280*, 1215–1218.

Gueguen, Y., and V. V. Palciauskas (1994), *Introduction to the Physics of Rocks*, 194 pp., Princeton Univ. Press, Princeton, N. J.

Hall, P. S., and C. Kincaid (2001), Diapiric flow at subduction zones: A recipe for rapid transport, *Science*, *292*, 2472–2475.

Hirth, G., and D. L. Kohlstedt (1996), Water in the oceanic upper mantle: Implications for rheology, melt extraction and the evolution of the lithosphere, *Earth Planet. Sci. Lett.*, *144*, 93–108.

Hofmann, A. W., and S. R. Hart (1978), Assessment of local and regional isotopic equilibrium in mantle, *Earth Planet. Sci. Lett.*, *38*, 44–62.

Holtzman, B. K., N. J. Groebner, M. E. Zimmerman, S. B. Ginsberg, and D. L. Kohlstedt (2003), Stress-driven melt segregation in partially molten rocks, *Geochem. Geophys. Geosyst.*, *4*(5), 8607, doi:10.1029/2001GC000258.

Jagoutz, O., O. Müntener, J.-P. Burg, P. Ulmer, and E. Jagoutz (2006), Lower continental crust formation through focused flow in km-scale melt conduits: The zoned ultramafic bodies of the Chilas complex in the Kohistan island arc (NW Pakistan), *Earth Planet. Sci. Lett.*, *242*, 320–342.

Jull, M., P. B. Kelemen, and K. Sims (2002), Consequences of diffuse and channelled porous melt migration on uranium series disequilibria, *Geochim. Cosmochim. Acta*, *66*, 4133–4148.

Kelemen, P. B., G. Hirth, N. Shimizu, M. Spiegelman, and H. J. B. Dick (1997), A review of melt migration processes in the adiabatically upwelling mantle beneath oceanic spreading ridges, *Philos. Trans. R. Soc. London Ser. A*, *355*, 283–318.

Khazan, Y., and Y. Fialko (2005), Why do kimberlites from different provinces have similar trace element patterns?, *Geochem. Geophys. Geosyst.*, *6*, Q10002, doi:10.1029/2005GC000919.

Kogiso, T., M. M. Hirschmann, and P. W. Reiners (2004), Length scales of mantle heterogeneities and their relationship to ocean island basalt geochemistry, *Geochim. Cosmochim. Acta*, *68*, 345–360.

McKenzie, D. (1985), ^{230}Th-^{238}U disequilibrium and the melting processes beneath ridge axes, *Earth Planet. Sci. Lett.*, *72*, 149–157.

McKenzie, D. (2000), Constraints on melt generation and transport from U-series activity ratios, *Chem. Geol.*, *162*, 81–94.

Nicolas, A. (1986), A melt extraction model based on structural studies in mantle peridotites, *J. Petrol.*, *27*, 999–1022.

Nicolas, A. and J. P. Poirier (1976), *Crystalline Plasticity and Solid State Flow in Metamorphic Rocks*, 444 pp., John Wiley, London.

Nye, J. F. (1953), The flow law of ice from measurements in glacier tunnels, laboratory experiments and the Jungfraufirn borehole experiment, *Proc. R. Soc. London, Ser. A*, *219*, 477–489.

Petford, N., D. Yuen, T. Rushmer, J. Brodholt, and S. Stackhouse (2005), Shear-induced material transfer across the core-mantle boundary aided by the post-perovskite phase transition, *Earth Planets Space*, *57*, 459–464.

Phipps Morgan, J., and B. K. Holtzman (2005), Vug waves: A mechanism for coupled rock deformation and fluid migration, *Geochem. Geophys. Geosyst.*, *6*, Q08002, doi:10.1029/2004GC000818.

Phipps Morgan, J., and W. J. Morgan (1999), Two-stage melting and the geochemical evolution of the mantle: A recipe for mantle plum-pudding, *Earth Planet. Sci. Lett.*, *170*, 215–239.

Plank, T., and C. H. Langmuir (1992), Effects of the melting regime on the composition of the oceanic crust, *J. Geophys. Res.*, *97*, 19,749–19,770.

Rabinowicz, M., and J.-L. Vigneresse (2004), Melt segregation under compaction and shear channeling: Application to granitic magma segregation in a continental crust, *J. Geophys. Res.*, *109*, B04407, doi:10.1029/2002JB002372.

Rabinowicz, M., P. Genthon, G. Ceuleneer, and M. Hillairet (2001), Compaction in a mantle mush with high melt concentrations and the generation of magma chambers, *Earth Planet. Sci. Lett.*, *188*, 313–328.

Renner, J., K. Viskupic, G. Hirth, and B. Evans (2003), Melt extraction from partially molten peridotites, *Geochem. Geophys. Geosyst.*, *4*(5), 8606, doi:10.1029/2002GC000369.

Ricard, Y., and D. Bercovici (2003), Two-phase damage theory and crustal rock failure: The theoretical 'void' limit, and the prediction of experimental data, *Geophys. J. Int.*, *155*, 1057–1064.

Richter, F. M., and D. McKenzie (1984), Dynamical models for melt segregation from a deformable rock matrix, *J. Geol.*, *92*, 729–740.

Rubin, A. M. (1998), Dike ascent in partially molten rock, *J. Geophys. Res.*, *103*, 20,901–20,919.

Rubin, K. H., I. van der Zander, M. C. Smith, and E. C. Bergmanis (2005), Minimum speed limit for ocean ridge magmatism from ^{210}Pb-^{226}Ra-^{230}Th disequilibria, *Nature*, *437*, 534–538.

Schmeling, H. (2000), Partial melting and melt segregation in a convecting mantle, in *Physics and Chemistry of Partially Molten Rocks*, edited by N. Bagdassarov et al., pp. 141–178, Kluwer Acad., Dordrecht, Netherlands.

Scott, D. R. (1988), The competition between percolation and circulation in a deformable porous-medium, *J. Geophys. Res.*, *93*, 6451–6462.

Scott, D. R., and D. J. Stevenson (1984), Magma solitons, *Geophys. Res. Lett.*, *11*, 1161–1164.

Scott, D. R., and D. J. Stevenson (1986), Magma ascent by porous flow, *J. Geophys. Res.*, *91*, 9283–9296.

Slater, L., D. McKenzie, K. Gronvold, and N. Shimizu (2001), Melt generation and movement beneath Theistareykir, NE Iceland, *J. Petrol.*, *42*, 321–354.

Sonder, L. J., P. C. England, and G. A. Houseman (1986), Continuum calculations of continental deformation in transcurrent environments, *J. Geophys. Res.*, *91*, 4797–4810.

Spiegelman, M. (1993), Flow in deformable porous-media.1. Simple analysis, *J. Fluid Mech.*, *247*, 17–38.

Spiegelman, M. (2003), Linear analysis of melt band formation by simple shear, *Geochem. Geophys. Geosyst.*, *4*(9), 8615, doi:10.1029/2002GC000499.

Spiegelman, M., and J. R. Reynolds (1999), Combined dynamic and geochemical evidence for convergent melt flow beneath the East Pacific Rise, *Nature*, *402*, 282–285.

Spiegelman, M., P. B. Kelemen, and E. Aharonov (2001), Causes and consequences of flow organization during melt transport: The reaction infiltration instability in compactible media, *J. Geophys. Res.*, *106*, 2061–2077.

Sumita, I., S. Yoshida, M. Kumazawa, and Y. Hamano (1996), A model for sedimentary compaction of a viscous medium and its application to inner-core growth, *Geophys. J. Int.*, *124*, 502–524.

Turner, S. P. (2002), On the time-scales of magmatism at island-arc volcanoes, *Philos. Trans. R. Soc. London, Ser. A*, *360*, 2853–2871.

Weinberg, R. F., and Y. Y. Podladchikov (1995), The rise of solid-state diapirs, *J. Struct. Geol.*, *17*, 1183–1195.

Wiggins, C., and M. Spiegelman (1995), Magma migration and magmatic solitary waves in 3-D, *Geophys. Res. Lett.*, *22*, 1289–1292.

————————————————

J. A. D. Connolly, Earth Sciences Department, ETH Zurich, 8092 Zurich, Switzerland. (james.connolly@erdw.ethz.ch)

Y. Y. Podladchikov, Physics of Geological Processes, University of Oslo, P.O. Box 1048, Blindern, Oslo, Norway.